Journal of Materials Research and Technology 39 (2025) 7613–7625

Contents lists available at ScienceDirect

Journal of Materials Research and Technology

journal homepage: www.elsevier.com/locate/jmrt

Balancing strength, modulus, and biocompatibility in a novel oxygen-containing β-type titanium alloy

Yazan Al-Zain [a,*], Masanari Sakato [b], Akiko Yamamoto [c], Jihad M. AlAjlouni [d], Mousa A. Al-Abbadi [e], Abdelkarim S. Aloweidi [f], Hee Young Kim [b,**]

[a] Department of Industrial Engineering, The University of Jordan, Amman, 11942, Jordan
[b] Department of Materials Science, University of Tsukuba, Tsukuba, Ibaraki, 305-8573, Japan
[c] Research Center for Functional Materials, National Institute for Materials Science, Tsukuba, Ibaraki, 305-0044, Japan
[d] Department of Orthopaedic Surgery, School of Medicine, The University of Jordan, Amman, 11942, Jordan
[e] Department of Pathology, Microbiology and Forensic Medicine, School of Medicine, The University of Jordan, Amman, 11942, Jordan
[f] Department of Anesthesia and Intensive Care, School of Medicine, The University of Jordan, Amman, 11942, Jordan

ARTICLE INFO

Handling Editor: SN Monteiro

Keywords:
β-Titanium alloy
Texture evolution
Ultralow elastic modulus
Biocompatibility
Orthopedic implants

ABSTRACT

Reducing the elastic-modulus mismatch between metallic implants and cortical bone remains a central challenge in orthopedic materials design. We report the development and evaluation of an oxygen-containing β-type titanium alloy, Ti–12Zr–6Nb–2Mo–2Sn–1.2O, engineered to combine high strength, ultralow modulus, and excellent biological performance. The oxygen was added to suppress the martensitic transformation and increase the strength of the Ti–12Zr–6Nb–2Mo–2Sn alloy. X-ray diffraction confirmed single-phase β stability without martensitic transformation across annealing treatments (1173 K, 60 s–1.8 ks). Texture and EBSD analyses revealed progressive weakening of the {110}⟨001⟩ with recovery and recrystallization. Tensile tests showed tunable responses: a favorable balance of low modulus (41 GPa) and high strength (>1000 MPa) at short annealing times, and increased ductility after prolonged annealing. Surface characterization indicated similar wettability and moderate roughness compared with cp-Ti; electrochemical tests confirmed stable passive-film formation and corrosion resistance. In vitro assays revealed enhanced fibroblast proliferation but reduced osteoblast adhesion relative to cp-Ti, indicating cell-type-dependent interactions. In vivo subcutaneous implantation in rats demonstrated tissue compatibility comparable to cp-Ti, with mild inflammation, successful regeneration, and normal hematopoiesis, albeit with slightly higher mast-cell degranulation. Collectively, Ti–12Zr–6Nb–2Mo–2Sn–1.2O is a promising low-modulus β-Ti alloy for load-bearing orthopedic implants; oxygen addition synergistically stabilizes the β phase and enhances mechanical performance while maintaining biocompatibility.

Abbreviations

Abbreviation	Meaning
XRD	X-ray Diffraction
ODF	Orientation Distribution Function
EBSD	Electron Backscatter Diffraction
IPF	Inverse Pole Figure
RD	Rolling Direction
TD	Transverse Direction
ND	Normal Direction
WCA	Water Contact Angle

(*continued on next column*)

(*continued*)

Abbreviation	Meaning
EIS	Electrochemical Impedance Spectroscopy
PDP	Potentiodynamic Polarization
SEM	Scanning Electron Microscopy
UTS	Ultimate Tensile Strength
Ra	Arithmetic Mean Roughness
Rt	Maximum Height Roughness
RPE	Relative Plating Efficiency
TCPS	Tissue Culture Polystyrene
cp-Ti	Commercially Pure Titanium

(*continued on next page*)

* Corresponding author.
** Corresponding author.
E-mail addresses: y.alzain@ju.edu.jo (Y. Al-Zain), heeykim@ims.tsukuba.ac.jp (H.Y. Kim).

https://doi.org/10.1016/j.jmrt.2025.11.120
Received 20 October 2025; Received in revised form 10 November 2025; Accepted 12 November 2025
Available online 13 November 2025

(*continued*)

Abbreviation	Meaning
FBS	Fetal Bovine Serum
E-MEM	Eagle's Minimum Essential Medium
CPE	Constant Phase Element
Rsol	Solution Resistance
Rct	Charge Transfer Resistance
TCPEdl	CPE Constant for Double Layer
pCPEdl	Exponent of CPE for Double Layer
ISO	International Organization for Standardization
MC3T3-E1	Mouse Calvaria-Derived Pre-Osteoblast Cell Line
L929	Mouse Fibroblast Cell Line
Ecorr	Corrosion Potential
Icorr	Corrosion Current Density
$I_{0.5}V$	Passivation Current Density at +0.5 V vs. Ag/AgCl
Ag/AgCl	Silver/Silver Chloride Electrode

1. Introduction

Titanium and its alloys are widely used for orthopedic and dental implants due to their unique combination of high specific strength, corrosion resistance, and favorable biocompatibility [1–4]. However, despite these advantages, Ti alloys have a significantly large mismatch in Young's modulus compared to natural bone, which can result in stress shielding and implant failure [5]. To overcome this limitation, alloy design strategies have focused on reducing the elastic modulus of titanium-based systems through compositional and microstructural control [6–8]. α- and (α+β)-type Ti alloys, such as Ti–6Al–4V, typically exhibit a high Young's modulus of about 110 GPa, much higher than that of bone (20–40 GPa), whereas β-type Ti alloys achieve substantially lower values (60–80 GPa) owing to their distinct elastic anisotropy and phase stability [9,10]. Consequently, recent research has shifted toward the development of metastable β-type Ti alloys with ultralow Young's modulus, achieved by adjusting the β phase stability using non-toxic elements such as Nb, Zr, Mo, and Sn [11–18].

A variety of metastable β-type titanium systems have been developed to overcome the modulus mismatch challenge, including Ti–Nb–Zr [11–13], Ti–Nb–Sn [15,16], and multi-component Ti–Zr–Nb–Sn–Mo alloys [19,20]. Alloying with β-stabilizing elements such as Nb, Zr, Sn, and Mo has been shown to effectively retain the single β phase, suppress the formation of brittle ω precipitates, and promote favorable recrystallization textures, leading to low Young's modulus values typically in the 40–55 GPa range. For instance, Kim et al. [19] demonstrated that a Ti–18Zr–5Nb–3Sn–2.5Mo alloy exhibits an ultralow modulus (~40 GPa) combined with high strength (776 MPa), excellent corrosion resistance, and in vivo biocompatibility, establishing it as a strong candidate for next-generation biomedical implants.

Beyond β stabilization, the role of interstitial elements has recently gained attention. Oxygen, often regarded as a harmful impurity, can simultaneously strengthen Ti alloys and maintain acceptable biological response when carefully controlled [21–25]. Similarly, Sn additions play a crucial role in suppressing ω-phase precipitation, thereby preventing embrittlement while maintaining ductility [6,26–28]. Recent modeling and experimental efforts confirm that fine-tuning electron-to-atom ratios (e/a), crystallographic texture, and interstitial concentrations are critical for optimizing mechanical compatibility [11,19,20,29,30]. Recent advances in β-Ti alloy design depend on electronic structure descriptors such as the bond order (Bo) and metal d-orbital energy level (Md) parameters. According to d-electron orbital theory, alloys positioned near the Ms = RT line on the Bo–Md map achieve optimal metastability, enabling stress-induced martensitic transformation and ultralow modulus. Xiao et al. [31] demonstrated this approach in Ti–40Zr–12Ta, where precise tuning of Bo ≈ 2.95 and Md ≈ 2.65 produced a β phase with E ≈ 72 GPa while maintaining a strength exceeding 1 GPa. In addition, Zhang et al. [32] simulated the $\beta \rightarrow \alpha''$ transformation in Ti–24Nb–4Zr–8Sn, revealing variant evolution that minimizes elastic strain energy, which supports the electronic-structure-driven pathway predicted by the d-orbital framework.

At the same time, corrosion resistance and biological performance remain decisive for clinical translation. Numerous β-Ti alloys, including Ti–16Nb–3Mo–1Sn [33], Ti–18Zr–Nb–Sn [34], and Ti–19Zr–10Nb–1Fe [35], have been shown to exhibit corrosion resistance and cytocompatibility comparable to cp-Ti. In vivo studies also demonstrate that Ti–15Zr–4Nb–4Ta alloy induces tissue responses similar to Ti–6Al–4V [36]. Recent reviews emphasize that modern alloy design must integrate both mechanical and biological perspectives to ensure reliable long-term performance [29,37–39].

Furthermore, compliance with international standards is essential for translational success. ISO 10993-5 provides the framework for *in vitro* cytotoxicity testing [40], while ISO 10993-2 establishes animal welfare requirements for in vivo biocompatibility studies [41]. These standards ensure that data on corrosion, cytocompatibility, and tissue response are consistent with global regulatory expectations. Clinical research has also confirmed that properly designed β-Ti alloys, when benchmarked against these standards, can effectively mitigate modulus mismatch while maintaining favorable host responses [42].

In this context, we developed and evaluated a novel oxygen-containing β-type alloy, Ti–12Zr–6Nb–2Mo–2Sn–1.2O. The design concept aimed to achieve: (i) an elastic modulus closer to cortical bone, (ii) high tensile strength (>1000 MPa), and (iii) excellent corrosion resistance and biocompatibility. Our preliminary results confirmed that the alloy exhibits high strength while maintaining a modulus in the range of 40–50 GPa, alongside favorable *in vitro* and in vivo biocompatibility compared with cp-Ti [19,33,34]. The present study builds upon the Ti–Zr–Nb–Sn–Mo family [19,20] and extends the alloy design approach by integrating controlled oxygen addition, offering a new pathway to balance mechanical and biological compatibility in next-generation implant alloys.

2. Methods

2.1. Preparation of test specimens

The Ti–12Zr–6Nb–2Mo–2Sn–1.2O alloy (in at. %) and commercially pure titanium (cp-Ti) ingots were synthesized through arc melting under an argon atmosphere. The raw materials used were pure Nb (99.9 %), Sn (99.99 %), Mo (99.9 %), TiO_2 (99.9 %), and pre-melted sponges of pure Ti (>99.7 %) and Zr (>99.6 %). The ingots were melted six times and flipped after each melting. The weight exhibited a negligible change, less than 0.05 %, before and after the melting process. Thus, the actual composition is regarded as being almost identical to the nominal composition. To ensure uniform composition, the alloy was homogenized at 1273 K for 2 h before cold rolling. Thickness reductions were 98.5 % for tensile and XRD tests, 80 % for in vivo studies, and 90 % for WCA, surface roughness, electrochemical, and cytotoxicity evaluations. The specimens were then precisely cut using an electric discharge-cutting machine, with dimensions tailored to specific tests: 2 mm × 2 mm × 15 mm for in vivo experiments, 10 mm × 10 mm × 1 mm for WCA, surface roughness, and cytotoxicity tests, and 15 mm × 15 mm × 1 mm for electrochemical measurements.

Following fabrication, the specimens were annealed at 1173 K for different times (60 s, 300 s, and 1.8 ks) and immediately quenched in water at room temperature to optimize the microstructure. To eliminate the oxide layer formed during heat treatment, the specimens were etched in a solution containing 50 % H_2O, 40 % HNO_3, and 10 % HF (vol %). Surface finishing was achieved through grinding up to 1200-grit SiC paper, followed by polishing with alumina paste (1 μm grain size) up to 3000 grit. After polishing, all specimens underwent ultrasonic cleaning in acetone for 10 min. Sterilization was performed using ethylene oxide gas (EOG) at 317 K for 23 h for *in vitro* studies, while autoclaving at 394 K for 15 min was applied for in vivo test specimens.

2.2. Microstructural observations

The constituent phases of the Ti–12Zr–6Nb–2Mo–2Sn–1.2O alloy were characterized by XRD using Cu Kα radiation (40 kV, 30 mA) over a 2θ range of 20–120° at room temperature. To further evaluate crystallographic texture, three incomplete pole figures of the {110}, {200}, and {112} planes of the β phase were measured using a conventional back-reflection method. The orientation distribution function (ODF) was reconstructed from these pole figures, and the corresponding inverse pole figures (IPFs) along the tensile direction were derived to assess orientation anisotropy. Electron backscatter diffraction (EBSD) was conducted in a scanning electron microscope (SEM) with an EBSD instrument at 15 kV, ~10–15 mm working distance, and step sizes of 0.2–0.5 μm. Scans were acquired on the specimens with the image x-axis parallel to RD, y-axis to TD, and the surface normal aligned with ND.

2.3. Tensile testing and elastic modulus evaluation

Uniaxial tensile tests were performed along the rolling direction (RD) using miniature dog-bone specimens (gauge length: 20 mm, width: 1.5 mm). Testing was conducted at a controlled strain rate of $2.5 \times 10^{-4}\ s^{-1}$, and at least three specimens were examined to ensure reproducibility. Strain evolution was captured using a high-resolution non-contact video extensometer (TRViewX, Shimadzu Corp.) equipped with dual tracking targets, enabling precise monitoring of gauge elongation without introducing mechanical interference. The Young's modulus was determined from the slope of the initial linear elastic regime of the stress–-strain curve, providing a direct measure of the alloy's elastic response under service-relevant loading conditions.

2.4. Water contact angle measurements

The wettability of both the alloy and cp-Ti was evaluated using static water contact angle (WCA) measurements, providing insights into the surface hydrophilicity and its potential impact on biocompatibility. The measurements were conducted using a contact angle meter (DM700, Kyowa Interface Science Co. Ltd. Japan) under ambient condition in a controlled humidity (50 ± 5 %) and temperature (298 ± 1 K) environment [43]. A sessile drop method was employed, where a 1 μL droplet of ultrapure water was gently dispensed onto the sample surface using an automated micro-syringe. The contact angle was measured at 2 s after droplet deposition using an image analysis software by fitting the droplet profile with the Young-Laplace equation. To ensure reproducibility, three measurements were taken at different locations on each specimen, and the final contact angle value was reported as the mean and standard deviation (SD).

2.5. Surface roughness measurements

The surface roughness of both materials was analyzed to evaluate its topographical characteristics and potential effects on wettability, cell adhesion, and overall biocompatibility. Measurements were performed using a confocal laser microscope (VK-9710, Keyence Corp. Japan) with a 50× objective lens giving the scanning area of 283× 212 μm^2, ensuring high-resolution characterization of surface features. The arithmetic mean deviation (R_a), and maximum height (R_t) were recorded, with three different locations measured per specimen to account for surface variability.

2.6. Electrochemical measurements

Electrochemical measurements were performed using a conventional three-electrode system and a potentiostat equipped with a frequency response analyzer (VersaSTAT4, Princeton Applied Research) to evaluate the corrosion behavior and passivation characteristics of the alloy. The working electrode (WE) consisted of the alloy or cp-Ti specimen with an exposed area of 0.899 cm^2, while a saturated Ag/AgCl electrode (3 M NaCl) was used as the reference electrode (RE) and a platinum mesh served as the counter electrode (CE). The electrolyte solution was a 10 mL portion of Eagle's minimum essential medium supplemented with 10 vol% fetal bovine serum (E-MEM+10 % FBS), maintained at 310 K under the atmosphere of 5 %CO_2 in humidified air to simulate physiological conditions.

Electrochemical impedance spectroscopy (EIS) was performed at the open circuit potential (OCP) with an alternating current (AC) amplitude of 10 mV in a frequency range from 10^{-2} to 10^5 Hz after immersion periods of 2 and 24 h. The obtained data were fitted with an equivalent circuit model using the Zview® software (version 4.0f, Scribner Associates Inc.).

Potentiodynamic polarization (PDP) tests were conducted by scanning the electrode potential from −0.25 V vs OCP to +1.8 V vs. Ag/AgCl at a scan rate of 0.5 mV/s after immersion periods of 0.5 and 24 h. The corrosion potential (E_{corr}) and corrosion current density (I_{corr}) were determined via Tafel extrapolation using the VersaStdio software (version 2.42.3, Princeton Applied Research). The current density at 0.5V (vs Ag/AgCl) was used as the parameter of passive current density ($I_{0.5V}$).

2.7. In vitro cytocompatibility tests

In vitro cytocompatibility tests were conducted using two cell lines: the murine fibroblasts L929 (NCTC Clone 929, CVCL_0462, purchased from Dainippon Pharmaceutical Col. Ltd.) and the murine osteoblastic cells MC3T3-E1 (CVCL_0409, purchased from Dainippon Pharmaceutical Col. Ltd.). Three specimens of both the alloy and the cp-Ti were placed in separate wells of two 24-well microplates: one each for L929 and MC3T3-E1. Then, 50 cells for L929 and 400 cells for MC3T3-E1 were inoculated onto the surface of each specimen with 1 mL of an appropriate culture medium (E-MEM+10 % FBS for L929 and α-modification of Eagle's MEM supplemented with 10 vol% FBS for MC3T3-E1). The inoculation number of cells for each cell lines were decided by pre-tests. Tissue culture polystyrene (TCPS) was used as a control material; three microplate wells without a specimen were employed for each type of cells. All microplates were kept in a humid incubator with 5 % CO_2 in air at 310 K for 7 days. After incubation, cells were fixed for 0.6 ks adding 125 μl of 25 % glutaraldehyde solution followed by rinsing with ultrapure water. Finally, cells were stained by 10 % Giemsa's solution for 0.9 ks, followed by rinsing with ultrapure water and air-dried.

The number of colonies having more than 50 cells were counted on the specimen and control wells. Relative plating efficiency (*RPE*) was calculated by the following equation;

$$RPE = \left(N_{sample} / A_{sample}\right) \ / \ \left(N_{control} / A_{control}\right)$$

where N_{sample} and $N_{control}$ indicate the number of colonies on the specimen surface and the bottom of the control well, respectively. A_{sample} and $A_{control}$ indicate the specimen top surface area and the bottom area of the control well (1.90 cm^2), respectively.

2.8. In vivo implantation tests

In vivo implantation tests were carried out following ethical guidelines for animal research, with approval from the Deanship of Scientific Research of the University of Jordan. In addition, the animal welfare requirements were followed strictly as per the ISO 10993-2 standard [44]. A total of 30 adult BALB/c rats (mean ± SD of mass as 179.6 ± 33.2 g) were used to assess the biocompatibility and tissue response of the newly synthesized alloy. The choice of BALB/c rats was based on their established suitability for subcutaneous implantation studies and their physiological response similarity to humans in biomaterial assessments [45].

The surgical implantation was conducted under aseptic conditions.

Anesthesia was induced using ketamine (50 mg/kg) and xylazine (5 mg/kg) intraperitoneally, ensuring minimal stress to the animals [46–48]. A bilateral dorsal subcutaneous implantation model was utilized, where each rat received one alloy specimen on the left dorsal side and a cp-Ti control on the right dorsal side. This intra-subject control model minimizes variability by accounting for individual immune responses.

Small incisions (~10 mm) were made, and subcutaneous pockets were carefully prepared using blunt dissection to prevent excessive trauma. Each specimen was inserted into the designated pocket, ensuring minimal movement post-implantation. The incisions were closed using absorbable sutures (5-0 Vicryl), and topical antiseptic (povidone-iodine) was applied. Postoperatively, animals were monitored in temperature-controlled cages with free access to food and water. Analgesia (buprenorphine, 0.05 mg/kg) was administered subcutaneously every 12 h for 48 h. Rats were labeled according to the English alphabetical letters from A to J (10 rats), A(Ti) used to designate the cp-Ti side of rat A and A(O) designated the alloy side of rat A. The same designation was used at 4, 8, and 12 weeks after implantation. Histological evaluations were carried out at 4-, 8-, and 12-week intervals post implantation. All wounds were clean with no evidence of wound infection at all intervals. Detailed procedure for the histological evaluation is described in the study by Al-Zain et al. [33].

2.9. Statistical analysis

All surface analysis and *in vitro* tests were performed in triplicate (n = 3 per condition), except electrochemical tests (n = 2) and in vivo implantation test (n = 10). Data were expressed as mean ± SD. Statistical analysis was carried out using one-way ANOVA with post-hoc Tukey's test, with $p < 0.05$ considered statistically significant.

2.10. Ethical approval

All animal procedures were conducted in accordance with the ethical standards of the University of Jordan and followed the guidelines of ISO 10993–2:2022 on animal welfare requirements. Adequate anesthesia, analgesia, and humane endpoints were applied to minimize animal discomfort.

3. Results and discussion

3.1. Microstructural observations

X-ray diffraction (XRD) patterns of the Ti–12Zr–6Nb–2Mo–2Sn–1.2O alloy annealed at 1173 K for 60 s, 300 s, and 1.8 ks (Fig. 1) confirmed the retention of a single β-phase structure across all conditions. Reflections were indexed to β(110), β(200), β(211), and β(220), with no evidence of martensitic α" phase. A minor shoulder near 34° was attributed to K_β radiation of the β(110) reflection rather than a secondary phase.

The β(110) reflection showed the highest intensity in all spectra. In combination with the pole-figure/ODF results shown later (Fig. 3), this corresponds to a pronounced {110}⟨001⟩ component or {110}⟨112⟩ component. With longer annealing durations, the diffraction peaks became sharper, consistent with recovery and recrystallization of the deformed β matrix.

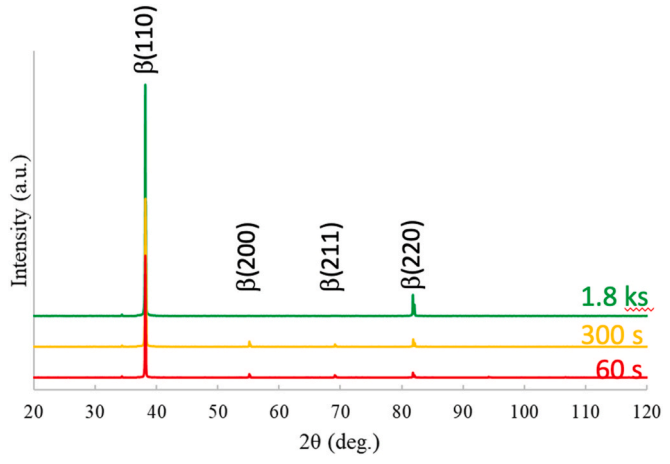

Fig. 1. X-ray diffraction (XRD) patterns of the Ti–12Zr–6Nb–2Mo–2Sn–1.2O alloy annealed at 1173 K for 60 s, 300 s, and 1.8 ks.

3.2. Mechanical properties

Uniaxial tensile tests performed along the rolling direction (RD) (Fig. 2) revealed that annealing time had a marked influence on the strength–modulus–ductility balance of the Ti–12Zr–6Nb–2Mo–2Sn–1.2O alloy. Table 1 summarizes the tensile properties of the Ti–12Zr–6Nb–2Mo–2Sn–1.2O alloy after different annealing times. The specimen annealed for 60 s exhibited the highest ultimate tensile strength (1062 ± 14 MPa) and the lowest elastic modulus (41.0 ± 1.1 GPa), indicating a strong β-phase texture with minimal recovery. This condition provided the most favorable combination of strength and low stiffness, closely matching the elastic response required to reduce stress shielding in orthopedic applications. At 300 s, the alloy revealed a moderate increase in modulus (47.9 GPa) and a decline in UTS (938 MPa) and ductility (7.7 %), consistent with partial recovery and subgrain coarsening. After 1.8 ks, recrystallization produced a more equiaxed microstructure, resulting in lower strength (860 ± 11 MPa) but improved ductility (10.7 ± 0.5 %), while the modulus increased to about 58 GPa. These trends confirm that extended annealing promotes softening and texture randomization, as discussed in Sections 3.4 and 3.5.

The mechanical trade-off here favors ductility and isotropy at the expense of strength and low stiffness.

Importantly, no stress-induced martensitic transformation was detected during loading across all conditions, confirming sufficient β-phase stability. The obtained modulus values (41–58 GPa) remain far lower than conventional α+β alloys such as Ti–6Al–4V (~110 GPa) [3,4] and are competitive with other metastable β-Ti biomedical alloys [11–20,37,38]. The high strength at short annealing times and the enhanced ductility after long annealing provide design flexibility depending on the target application. The progressive changes in modulus, strength, and ductility align with the texture evolution discussed in Sections 3.4–3.5. Since the alloy annealed at 1173 K for 60 s exhibited the most favorable balance of mechanical properties, namely the lowest elastic modulus (~41 GPa) and the highest ultimate tensile strength (>1000 MPa), all subsequent surface, electrochemical, and

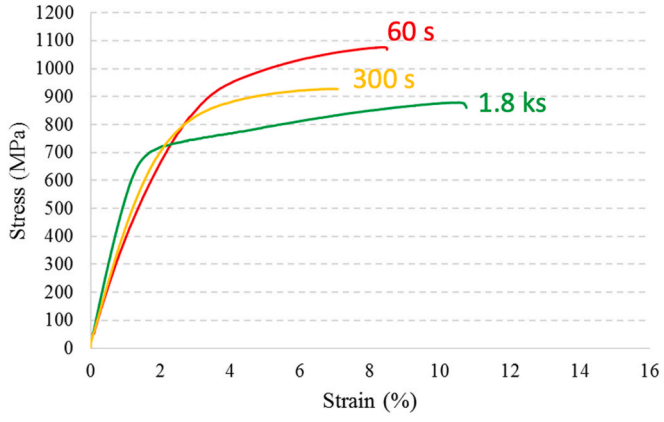

Fig. 2. Representative tensile stress–strain curves of the Ti–12Zr–6Nb–2Mo–2Sn–1.2O alloy annealed at 1173 K for 60 s, 300 s, and 1.8 ks.

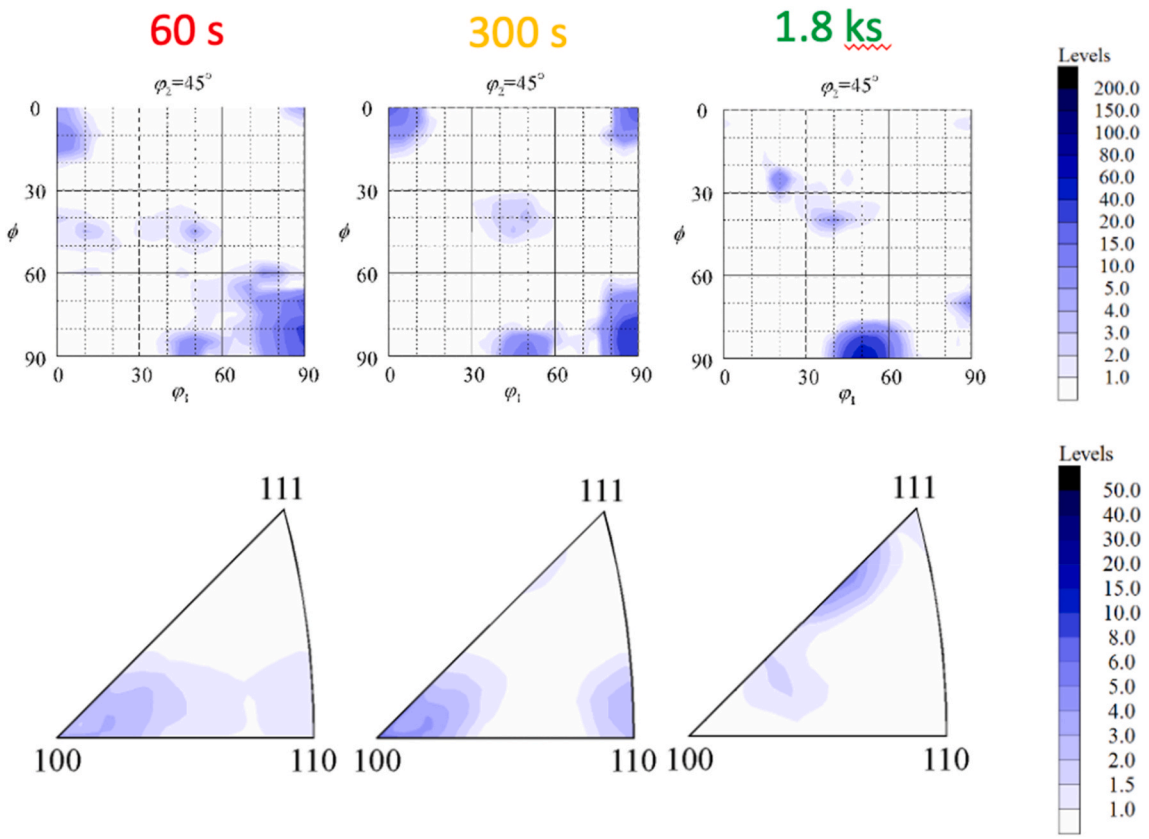

Fig. 3. Pole figures (top row) and inverse pole figures (bottom row) of the Ti–12Zr–6Nb–2Mo–2Sn–1.2O alloy annealed at 1173 K for 60 s, 300 s, and 1.8 ks.

Table 1
Tensile properties of the Ti–12Zr–6Nb–2Mo–2Sn–1.2O alloy annealed at 1173 K for different times (60 s, 300 s, and 1.8 ks)

Annealing time	Young's Modulus (GPa)	UTS (MPa)	Elongation (%)
60 s	41.0 ± 1.1	1062 ± 14	8.9 ± 0.8
300 s	47.9 ± 3.9	938 ± 14	7.7 ± 1.1
1.8 ks	58.0 ± 4.1	860 ± 11	10.7 ± 0.5

biological evaluations (Sections 3.8 onward) were conducted on specimens prepared under this condition.

3.3. Effect of oxygen addition

The addition of ~1.2 at.% O contributed primarily to solid-solution strengthening and had a stabilizing influence on the β-phase matrix. Oxygen is known to increase the yield strength and the ultimate tensile strength while maintaining sufficient elongation [23–25]. As shown in Fig. S1 and Table S1, the increase in oxygen content increases the yield strength and ultimate tensile strength of the Ti–12Zr–6Nb–2Mo–2Sn alloy. Increased oxygen content reduces the elongation of the Ti–12Zr–6Nb–2Mo–2Sn alloy; however, it is noteworthy that elongation exceeding 10 % is maintained with a 1.2 at.% O addition. The ductility of the Ti–12Zr–6Nb–2Mo–2Sn–1.5O alloy deteriorates markedly. This behavior aligns with previous findings on oxygen-modified Ti–based alloys, where interstitial O enhances strength while maintaining acceptable plasticity [24,25]. Such dual functionality, mechanical strengthening and phase stabilization, complements the recrystallization and texture evolution discussed in Section 3.4, collectively explaining the observed strength–ductility balance.

3.4. Texture evolution and annealing time

Pole figure and ODF analyses (Fig. 3) revealed that the specimens annealed at 1173 K retained a pronounced {110}⟨001⟩ texture at 60 s. At 300 s, in addition the primary {110}⟨001⟩ component, {110}⟨112⟩ and {001}<110> components became more evident. At 1.8 ks, however, the major component was changed to {110}<112>.

Texture evolution exhibited clear directional dependence, as confirmed by the EBSD IPF maps (Fig. 4) in relation to the ODF results (Fig. 3). The EBSD analysis verified the change in major texture components observed by XRD: while the {110}⟨001⟩ orientation dominated at 60 s, it gradually transformed into a {110}⟨112⟩ component after prolonged annealing (1.8 ks). {110}⟨001⟩ grains appear red in the RD-IPF map and green in the ND-IPF map, on the other hand, {110}⟨112⟩ grains appear pink–purple in the RD-IPF map and green in the ND-IPF map, enabling visual confirmation of this transition.

At 60 s, the microstructure was composed of fine, strain-recovered β-grains with a strong {110}⟨001⟩ texture. This structural state provided the most favorable combination of high strength and low elastic modulus due to oxygen solid-solution hardening coupled with texture-induced elastic softening along RD. By 1.8 ks, extensive secondary recrystallization and grain growth had occurred, producing a coarser and more equiaxed β-structure dominated by the {110}⟨112⟩ orientation. This progressive change reflects the combined effects of recovery, recrystallization, and orientation rotation during texture redistribution.

Overall, the EBSD results confirm the microstructural and textural evolution indicated by the ODF analysis, demonstrating that the transformation from {110}⟨001⟩ to {110}⟨112⟩ with increasing annealing time governs the balance between strength, ductility, and elastic anisotropy in the Ti–12Zr–6Nb–2Mo–2Sn–1.2O alloy [41,42].

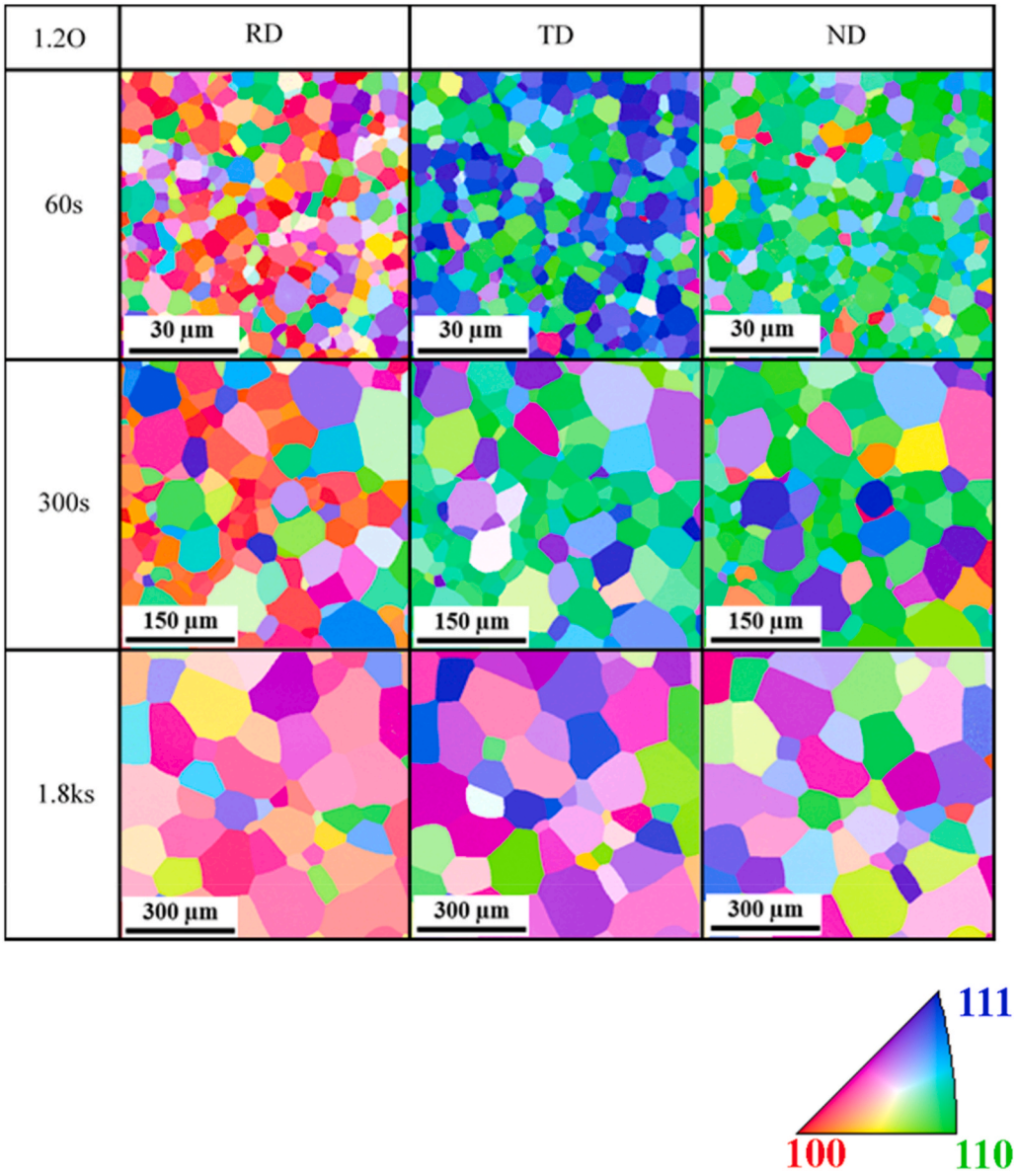

Fig. 4. EBSD inverse pole figure (IPF) maps of the Ti–12Zr–6Nb–2Mo–2Sn–1.2O alloy annealed at 1173 K for 60 s, 300 s, and 1.8 ks along rolling direction (RD), transverse direction (TD), and normal direction (ND).

3.5. Mechanistic interpretation and implications for mechanical anisotropy and biomedical applications

The combined microstructural and textural evolution discussed in the previous sections provides a mechanistic basis for understanding the observed mechanical anisotropy and its biomedical relevance. The texture evolution can be attributed to recovery, recrystallization, and selective grain growth, which progressively broaden the orientation distribution. Grain boundary migration favors misoriented grains with lower stored energy, promoting orientation randomization particularly in TD and ND. The concurrent additions of Sn and O stabilize the β phase throughout this process, effectively suppressing martensitic transformation even at extended annealing times. This synergistic alloy design strategy highlights a pathway to simultaneously control phase stability, grain growth, and texture evolution in biomedical β-Ti alloys.

The resulting anisotropic texture has direct implications for both elastic and plastic responses. The strong {110}⟨001⟩ texture along RD minimizes the modulus in this direction, as the ⟨001⟩ crystallographic direction—known to be the softest elastic axis in bcc metals, including β-Ti [7,8]—offers the lowest elastic stiffness. With increasing annealing time, the progressive weakening of this texture reduces anisotropy but slightly increases the average modulus. By tailoring the balance between texture retention along RD and controlled recrystallization, it is possible to achieve both structural isotropy and a desirable low-modulus response.

From a biomedical standpoint, this controllable anisotropy is highly beneficial for load-bearing implant design. A preferentially oriented β-phase structure can provide reduced modulus along the loading direction, minimizing stress shielding while preserving sufficient strength. Meanwhile, the suppression of the martensitic phase formation ensures mechanical stability and corrosion resistance under physiological conditions. Thus, the Ti–12Zr–6Nb–2Mo–2Sn–1.2O alloy demonstrates how compositional and thermomechanical design can be integrated to achieve simultaneous optimization of texture, phase stability, and mechanical compatibility for next-generation orthopedic and dental implants.

3.6. Contact angle measurements

The wettability of the alloy and cp-Ti was assessed through water contact angle (WCA) measurements, as summarized in Table 2. The average contact angle for the alloy was 70.9°, while the cp-Ti exhibited a slightly higher WCA of 72.6° [33]. These values indicate that both materials exhibit similar hydrophilicity, with no drastic changes in wettability induced by the compositional modification.

To determine the statistical significance of this difference, an F-test and T-test were performed. The F-test value of 0.499 indicates comparable variance between the two datasets, supporting the validity of the T-test result. The T-test p-value of 0.518 suggests that the difference between the contact angles of the alloy and the cp-Ti is not statistically significant ($p > 0.05$), implying that the compositional modification did not lead to a substantial alteration in wettability. The results indicate only a marginal decrease in WCA, which is statistically insignificant. This suggests that the native oxide layer of cp-Ti already provides a hydrophilic surface, and the compositional modification does not introduce a significant enough change in surface chemistry to further enhance wettability. The minor reduction in WCA may still be attributed to subtle variations in oxide layer thickness, electronic structure, or microstructure, but these effects appear to be minimal.

Because surface wettability affects protein adsorption and cell adhesion, the observed similarity between cp-Ti and the alloy indicates that both surfaces should exhibit comparable biocompatibility in practice. Therefore, differences in biological response (S ection 3.11) are unlikely to arise from hydrophilicity alone but are more likely related to combined effects of surface roughness, oxide chemistry, and protein adsorption.

3.7. Surface roughness measurements

The surface roughness of the alloy and the cp-Ti was evaluated using multiple roughness parameters, including the arithmetic mean deviation (R_a), and maximum height (R_t). The results, shown in Table 3, indicate notable differences in surface topography between the two materials, suggesting that the compositional modification influences surface morphology.

The R_a (mean roughness) values were 0.118 μm for the alloy and 0.148 μm for cp-Ti [33]. Although the difference is relatively small, cp-Ti shows a significantly higher R_a, suggesting a more pronounced surface texture compared to the alloy. However, the R_t (mean peak-to-valley height) values were similar to each other; 1.71 μm for the alloy and 1.88 μm for cp-Ti [33].

The slight reduction in roughness for the alloy compared to cp-Ti may contribute to the observed lower water contact angle, supporting the hypothesis that smoother surfaces tend to exhibit better wettability [49]. However, since the difference in roughness is minimal, the impact on hydrophilicity remains relatively minor, aligning with the statistically insignificant change in water contact angle observed in previous WCA analysis.

Surface roughness plays a crucial role in determining cell adhesion, osteoblast activity, and implant integration. Studies have shown that moderate roughness (R_a ~0.1–0.3 μm) enhances cell adhesion, whereas excessively smooth or rough surfaces may hinder optimal biological interactions [50]. Given that both cp-Ti and the alloy fall within this range, they are expected to exhibit similar biological responses, with the alloy potentially offering slightly improved surface characteristics due to its combination of smoothness and wettability. These results connect directly with the cytocompatibility findings (S ection 3.11), as the slightly smoother surface of the alloy may enhance fibroblast adhesion while providing less favorable conditions for osteoblast attachment, partly explaining the divergent cell behaviors.

Table 2
Water contact angle data of the alloy and the cp-Ti.

Material	Mean WCA (°)	Standard Deviation (°)	F-Test	T-Test	Ref.
the alloy	70.9	2.12	0.499	0.518	
cp-Ti	72.6	3.68	–	–	[33]

Table 3
Surface roughness data of the alloy and cp-Ti.

Material	Mean R_a (μm)	Standard deviation of R_a (μm)	Mean R_t (μm)	Standard deviation of R_t (μm)	Ref.
The alloy	0.118	0.014	1.71	0.24	
cp-Ti	0.148	0.002	1.88	0.19	[33]
F-Test	**0.032**	–	0.774	–	
T-Test	**0.061**	–	0.388	–	

3.8. Electrochemical measurements

3.8.1. Electrochemical impedance spectroscopy

The typical Nyquist plots of the EIS results are presented in Fig. 5 with the equivalent circuit model employed for the data fitting. The parameters obtained by the fitting of EIS data are displayed in Table 4. For both the materials, the impedance increased with the immersion periods. For both 2 and 24 h of the immersion periods, the impedance of cp-Ti was slightly higher than that of the alloy. As shown in Table 4, R_{sol}, the resistance of the electrolyte, was around 25 Ω cm^2 for both materials and both immersion periods. The R_{ct}, the resistance for charge transfer, was higher for cp-Ti at both 2 and 24 h immersion, though no statistical significance was confirmed. This suggests the slightly better corrosion resistance of the cp-Ti in this experimental condition than that of the alloy, but their difference is not significant.

The T_{CPE} and p_{CPE} indicate the constant and exponent of constant phase element (CPE) for the electric double layer, where the cp-Ti specimens have significantly lower constant and higher exponent than those of the alloy at the corresponding time periods. The higher T_{CPEdl} of the alloy at 2 and 24h did not depend on the higher surface area because

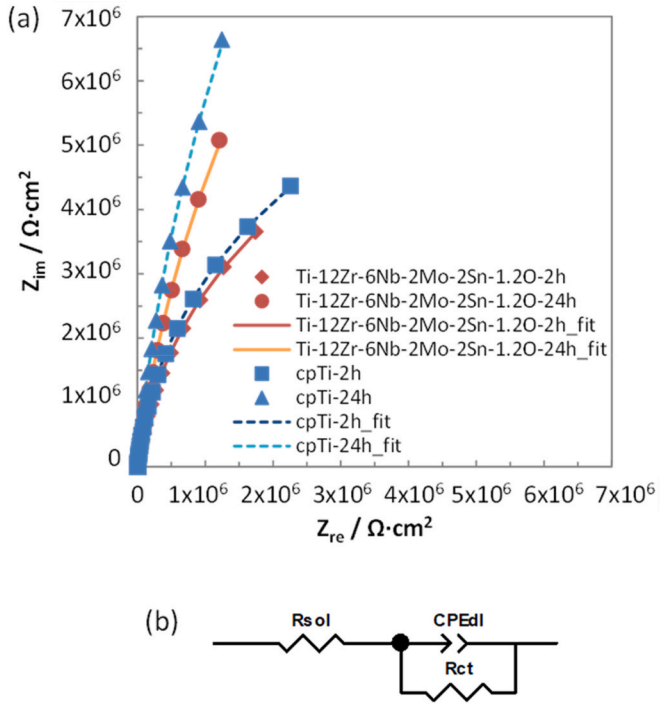

Fig. 5. Typical Nyquist plots of EIS data for the alloy and cp-Ti (a) and the equivalent circuit model employed for fitting (b).

Table 4
Parameters obtained by the fitting of EIS data with an equivalent circuit model.

	Time (h)	Mean R_{sol} ($\Omega \cdot cm^2$)	SD of R_{sol} ($\Omega \cdot cm^2$)	Mean R_{ct} ($\Omega \cdot cm^2$)	SD of R_{ct} ($\Omega \cdot cm^2$)	Mean T_{CPEdl} ($F \cdot S^{p-1} \cdot cm^2$)	SD of T_{CPEdl} ($F \cdot S^{p-1} \cdot cm^2$)	Mean p_{CPEdl}	SD of p_{CPEdl}
The alloy (n = 2)	2	24.1	11.2	1.26×10^6	7.07×10^3	2.76×10^{-5}	1.93×10^{-6}	0.920	0.004
	24	23.3	10.7	2.69×10^6	2.15×10^6	2.33×10^{-5}	1.23×10^{-6}	0.924	0.005
cp-Ti (n = 3)	2	27.3	4.13	8.28×10^6	6.10×10^6	2.17×10^{-5}	2.86×10^{-6}	0.946	0.002
	24	26.3	4.13	1.28×10^7	5.77×10^6	1.80×10^{-5}	1.89×10^{-6}	0.952	0.003
F-test	2	0.226	–	0.002	–	0.863	–	0.416	–
	24	0.244	–	0.509	–	0.839	–	0.454	–
T-test	2	0.665	–	0.184	–	**0.087**	–	**0.003**	–
	24	0.668	–	0.108	–	**0.042**	–	**0.005**	–

R_{sol} and R_{ct} indicates the resistance for the electrolyte and the charge transfer. T_{CPE} and p_{CPE} indicate the constant and exponent of constant phase element (CPE) for the electric double layer (*dl*).

the R_a of the specimen surface was significantly smaller for the alloy than the cp-Ti, as described on Table 3. T_{CPEdl} value also decreased with increase in immersion period for both materials, suggesting the chronological change in specimen surface condition through the immersion in the E-MEM+10 % FBS. Since E-MEM+10 % FBS contains various inorganic ions as well as organic components such as proteins, adsorption of these components may influence the electric charge on the specimen surface. Because the alloy exhibited comparable passive film stability to cp-Ti, the differences in osteoblast adhesion observed *in vitro* (S ection 3.11) are unlikely due to corrosion or ion release, but instead may be linked to subtle variations in oxide composition and protein adsorption dynamics.

3.8.2. Potentiodynamic polarization

The typical potentiodynamic polarization curves for cp-Ti and the alloy in E-MEM+10 %FBS are shown in Fig. 6. As shown in Table 5, the corrosion potential (E_{corr}) for cp-Ti after 0.5 h of immersion was −226 mV vs. Ag/AgCl, whereas the alloy exhibits a slightly lower E_{corr} of −268 mV vs. Ag/AgCl. The more negative E_{corr} of the alloy suggests a slight thermodynamic disadvantage in resisting initial oxidation compared to cp-Ti. The alloy also gives the slightly higher corrosion current density (I_{corr}) as 74.0 nA/cm^2 than that of cp-Ti (28.8 nA/cm^2). However, the passivation current density ($I_{0.5v}$), which represents the stability of the passive oxide layer, is slightly lower for the alloy (724 nA/cm^2) than cp-Ti (758 nA/cm^2). This lower $I_{0.5v}$ value indicates that the alloy forms a stable and protective passive film in slightly better level to cp-Ti. The low $I_{0.5}$ value typically correlates with better resistance to passive film breakdown and reduced risk of localized corrosion, such as pitting or crevice corrosion. This indicates that the alloy maintains a more stable passive state even under anodic polarization at the initial stage of immersion, making it suitable for biomedical applications where long-term exposure to physiological environments requires strong corrosion resistance.

After 24 h of immersion, the E_{corr} for the cp-Ti was −242 mV vs Ag/AgCl, which was slightly negative than that at 0.5 h of immersion. For the alloy, however, E_{corr} after 24 h of immersion was −173 mV vs Ag/AgCl, which is slightly positive from that at 0.5 h of immersion. For both materials, the I_{corr} at 24 h decreased in comparison with those at 0.5 h. As shown in Fig. 6, the cathodic curve of the alloy specimen was almost identical for 0.5 h and 24 h, while the current density between E_{corr} to 0.3V vs Ag/AgCl was drastically decreased from 0.5 h to 24 h. For the cp-Ti, however, the current density decreased both cathodic and anodic (E_{corr} to 0.3V vs Ag/AgCl) regions. This difference in the reduction of cathodic reaction could results in the negative shift of the E_{corr} for the cp-Ti. For both materials, the $I_{0.5v}$ at 24 h was over 1 mA/cm^2, which significantly increased from those at 0.5 h. As described in the previous section, the EIS data suggest the change in the surface condition with increase in immersion period, which may be due to the adsorption of the ingredients of E-MEM+10 % FBS. This can be responsible for the increase in $I_{0.5}v$. Oxide layer formed during the immersion in E-MEM+10 % FBS may contain adsorbed ingredients, reducing the quality as the passive layer. Therefore, this mixed layer resulted in the higher passivation current density than the initial stage of the immersion.

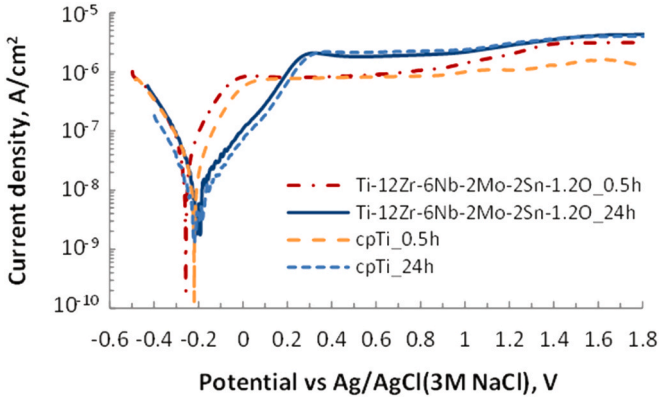

Fig. 6. Typical potentiodynamic polarization curves for the alloy and cp-Ti.

3.9. In vitro cytocompatibility tests

The cytocompatibility of cp-Ti and the alloy was evaluated by colony formation assays using L929 and MC3T3-E1. Typical macroscopic images of the specimens after staining the colonies are shown in Fig. 7, and results are summarized in Fig. 8.

For L929, the colony counts (mean ± SD) observed on control (TCPS), cp-Ti, and the alloy was 15.6 ± 2.9, 15.0 ± 4.4, and 19.7 ± 3.1, respectively. This translates to *RPE* of 0.96 ± 0.28 for cp-Ti and 1.26 ± 0.20 for the alloy. The increased *RPE* for the alloy suggests enhanced fibroblast adhesion and proliferation, indicating a more favorable surface for cellular attachment and growth. However, there was no statistical significance between the cp-Ti and the alloy ($p > 0.1$ by student's t-test).

For MC3T3-E1, the colony counts (mean ± SD) for TCPS, cp-Ti, and the alloy were 20.2 ± 0.6, 20.3 ± 2.5, and 15.3 ± 0.6, respectively. The corresponding *RPE* values were 1.01 ± 0.12 for cp-Ti and 0.76 ± 0.03 for the alloy ($p < 0.01$ by student's t-test). Unlike the fibroblast results, MC3T3-E1 exhibited reduced adhesion and proliferation on the alloy, suggesting a less favorable surface environment for osteoblast attachment compared to cp-Ti. This behavior may be attributed to surface topography, oxide layer composition, and corrosion during the cell culture that could influence the response of osteoblastic cells.

The surface physicochemical properties of Ti alloys depend on the surface oxide composition, which is influenced by the alloy composition and microstructure. In case of the binary Ti–Zr alloys, the Zr concentration in the oxide layer increased with increase in Zr content of the alloy [51,52]. The incorporation of Zr into the oxide layer increases hydrophilicity of the surface, decreasing static contact angle of a water droplet [53]. The change in surface hydrophilicity influences protein adsorption behavior; albumin adsorption tended to increase with

Table 5
Corrosion Parameters obtained from PDP for cp-Ti and the alloy.

Material	Time (h)	Corrosion Potential (E_{corr}, mV vs Ag/AgCl)	Standard deviation of E_{corr} (mV)	Corrosion Current Density (I_{corr}, nA/cm^2)	Standard deviation of I_{corr} (nA/cm^2)	Passivation Current Density ($I_{0.5v}$, (nA/cm^2)	Standard deviation of $I_{0.5v}$ (nA/cm^2)
The alloy	0.5	−268	17.6	74.0	16.4	724	65.6
	24	−173	10.2	19.2	6.2	1901	134
cp-Ti	0.5	−226	10.8	28.8	6.6	758	41.5
	24	−242	37.8	3.8	3.6	1683	575
F-test	0.5	0.701	–	0.447	–	0.718	–
	24	0.374	–	0.447	–	0.325	–
T-test	0.5	0.096	–	**0.035**	–	0.650	–
	24	0.103	–	**0.070**	–	0.601	–

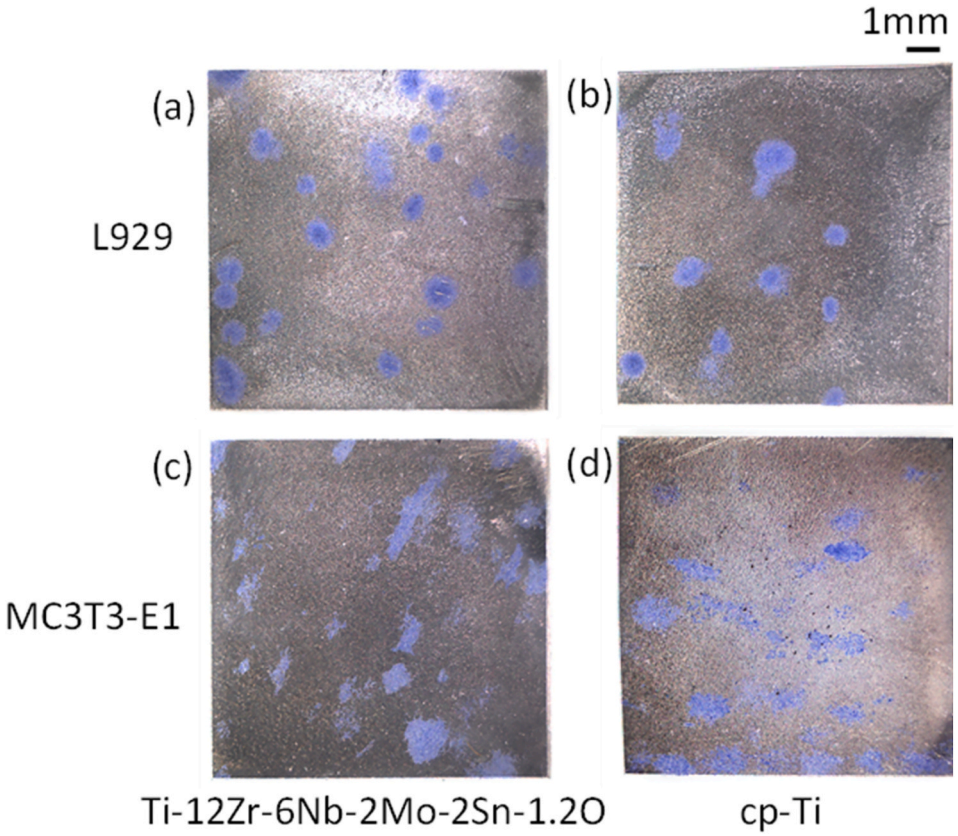

Fig. 7. Examples of macroscopic images of the specimens after staining the colonies by Giemsa's stain into blue. (a), (c); Ti–12Zr–6Nb–2Mo–2Sn-1.2O, and (b), (d): cp-Ti for (a), (b): L929 and (c), (d): MC3T3-E1.

increase in Zr content of the alloy [52]. Albumin, a common protein in blood plasma, is not involved in cell adhesion onto material surface, but its adsorption onto material surface interferes with adsorption of other proteins such as fibronectin or laminin, which are mandatory for cell adhesion and growth. The necessary "adhesive" proteins are depending on the types of cells; therefore, different cells show different adhesion and growth behavior on the material surface. Previous studies reported the decrease in the adhesion of murine osteoblast MC3T3-E1 onto Ti–Zr alloys with increase in Zn content in the alloy [53]. Addition of other alloying elements also influences the biocompatibility of the Ti alloys. Nb addition is known to stabilize the passivity of the surface oxide film incorporated as Nb_2O_5 [54]. The increase of Nb content in the Ti-x%Nb–%5Sn alloy increases hydrophobicity of the surface, increasing contact angle of an artificial saliva droplet as 82.4–93.9° [54]. However, the proliferation of MC3T3-E1 on Ti–40 %Nb and Ti–10 %Nb–5 %Sn was reported as lower than that of cp-Ti after 4–12 days of culture [55], as the optimal surface hydrophilicity/hydrophobicity for cell adhesion is peaked around 70° in static water contact angle [56].

Y.J. Park et al. investigated the effect of alloying elements on cell viability of L929 after 24h of incubation using binary Ti alloys containing up to 20 % of alloying elements [57]. They reported most of the alloys have relative cell viability over 80 %, indicating the alloy with Ti content over 80 % has good cytocompatibility. In the present study, the Ti content of the alloy is slightly lower than 80 %, but it has a good cell growth of L929 after 7 d of incubation.

Our previous study reported the cytocompatibility of Ti–18Zr–5Nb–3Sn-2.5Mo alloy for L929 and MC3T3-E1 as the similar level to cp-Ti [19]. The alloy in the present study somewhat has a close composition except O, but the cell growth of MC3T3-E1 was significantly lower than that of cp-Ti. Interestingly, F. B. Vicente et al. investigated the influence of small quantities of O in Ti–Zr alloys on the proliferation of MC3T3-E1, reporting the drop of cell viability at a certain concentration of O in the alloy, e.g. 0.39 % for Ti–10 %Zr alloy and 0.31 % for Ti–5 %Zr alloy [21]. The lower cell growth of MC3T3-E1 on our tested alloy may be related to the O addition. For multi-element alloys, it is difficult to assign the influence of alloying elements on its biocompatibility, but it can be noted that the cytocompatibility test results includes the influences of multiple factors such as surface

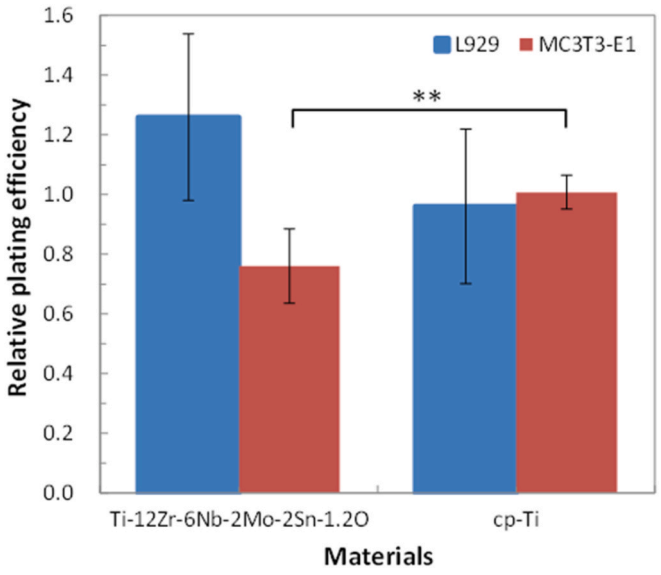

Fig. 8. The Relative plating efficiency (RPE) for both cell lines of the cp-Ti and the alloy. (**p < 0.05 by student t-test in comparison to cp-Ti).

physicochemical properties, oxide layer composition, and microstructures in a complex manner.

The results of *in vitro* cytocompatibility reveal that the alloy exhibits superior fibroblast adhesion, but reduced osteoblast attachment compared to cp-Ti. These findings suggest that the alloy may be better suited for applications requiring fibroblast integration, such as soft tissue interfaces, rather than direct bone-contact applications where cp-Ti may remain more effective. Further studies using surface functionalization, protein adsorption analysis, and long-term cell viability assays could provide deeper insights into optimizing the material for specific biomedical uses. While osteoblast adhesion was reduced on the alloy, the favorable fibroblast proliferation suggests suitability for applications involving soft tissue integration. Importantly, these *in vitro* observations should be interpreted in the context of the in vivo results (Section 3.10), where overall tissue compatibility remained excellent.

3.10. *In vivo biocompatibility tests*

The subcutaneous implantation study was conducted using 30 BALB/c rats to evaluate the biocompatibility of the control material (cp-Ti) and the alloy. The implantation was performed under intraperitoneal Ketamine anesthesia (50 mg/kg), with the tested alloy inserted on the right side and the cp-Ti on the left side. The study followed ISO 10993-2 guidelines for biocompatibility assessment [44].

Postoperative monitoring showed no adverse reactions, no wound infections, and no mortality across the experimental period, demonstrating the initial safety of both materials. The animals were euthanized at 4-, 8-, and 12-weeks post-implantation for histological analysis.

3.10.1. *Histological analysis of tissue responses: capsule formation and tissue response*

Fig. 9a presents a histological section from rat A1 (control, cp-Ti) at 12 weeks, showing the skin epidermis, dermis, underlying capsule, and subcutaneous tissue. The presence of a fibrous capsule (bi-headed arrow) indicates a typical foreign body reaction with no evidence of excessive fibrosis or necrosis, suggesting a biocompatible interaction with host tissues.

3.10.2. *Inflammatory response and immune cell infiltration*

The immune response was assessed at multiple time points, revealing a progressive adaptation of host tissue to the implants. At 4 weeks (Fig. 9b, rat B1, cp-Ti), a reactive lymph node was observed, signifying an early-stage immune response, which is typical post-implantation and does not necessarily indicate severe inflammation. By 8 weeks (Fig. 9c, rat C1, cp-Ti), an increase in mast cell presence was noted, suggesting a continued immune response, though still within an expected range. At 12 weeks (Fig. 9d, rat I1, cp-Ti), only a few neutrophilic bands remained, indicating minimal residual inflammation, demonstrating that the tissue had successfully adapted to the implant.

For the alloy, a notable difference emerged at 12 weeks (Fig. 9e, rat B2, the alloy), where mast cells appeared degranulated, suggesting a more active immune response, potentially due to surface reactivity or ion release. Mast cell plays an important role in immune response to parasite infection but often induces Type I allergy with IgE binding allergen. However, metal allergy, caused by released meal ions as haptens, is classified to Type IV (delayed type hypersensitivity), which involves Th1 cell. Therefore, the cause of mast cell activation is unclear, but chronic reaction can cause tissue/organ damages, warranting further long-term evaluation.

3.10.3. *Tissue regeneration and fat deposition*

At 8 weeks (Fig. 9f, rat I2, the alloy), a brown fat section was identified, indicating healthy tissue remodeling with no signs of necrosis, suggesting a stable healing response. By 12 weeks (Fig. 9g, rat G2, the alloy), normal bone marrow with active hematopoiesis was observed, confirming that the implant did not induce systemic adverse effects. Additionally, at 8 weeks (Fig. 9h, rat J2, the alloy), the skeletal muscle morphology remained intact, demonstrating good integration without muscle degradation, further supporting the biocompatibility of the alloy.

Both cp-Ti and the alloy demonstrated good biocompatibility, with similar levels of fibrosis and mild inflammation; however, the alloy exhibited slightly higher mast cell degranulation, indicating increased immune reactivity. Tissue regeneration was successful for both materials, with no necrosis, granulomas, or severe immune responses, while the presence of brown fat and normal hematopoiesis in the alloy suggests no disruption to systemic functions. These findings support the potential use of the alloy in biomedical applications, though its higher mast cell activity warrants further long-term evaluation to confirm implant stability and potential low-level immune interactions. The generally favorable in vivo outcomes, despite reduced osteoblast adhesion *in vitro*, indicate that long-term biological integration may not be hindered. This highlights the importance of combining *in vitro* and in vivo approaches, and suggests that initial cell-level disadvantages may be compensated by systemic tissue remodeling processes.

4. Conclusion

The Ti–12Zr–6Nb–2Mo–2Sn–1.2O alloy demonstrated a unique synergy between phase stability, tailored texture evolution, and promising biological response. XRD and ODF analyses confirmed the persistence of a single β phase, with a strong {110}⟨001⟩ that gradually weakened under annealing but retained sufficient anisotropy to sustain a low Young's modulus (~41–58 GPa). Among all conditions, the specimen annealed at 1173 K for 60 s showed the most favorable performance, combining the lowest elastic modulus (~41 GPa) with the highest ultimate tensile strength (>1000 MPa), providing the closest match to cortical bone. Oxygen addition effectively enhanced β-phase stability and strength without sacrificing ductility.

Surface analyses highlighted comparable wettability and roughness to cp-Ti, while electrochemical testing demonstrated stable passive film formation under physiological conditions. In vitro assays revealed favorable fibroblast proliferation and acceptable osteoblast interactions, whereas in vivo implantation confirmed successful tissue integration with only mild immune reactivity.

Overall, Ti–12Zr–6Nb–2Mo–2Sn–1.2O is a strong candidate for load-bearing orthopedic implants, addressing the dual challenge of reducing

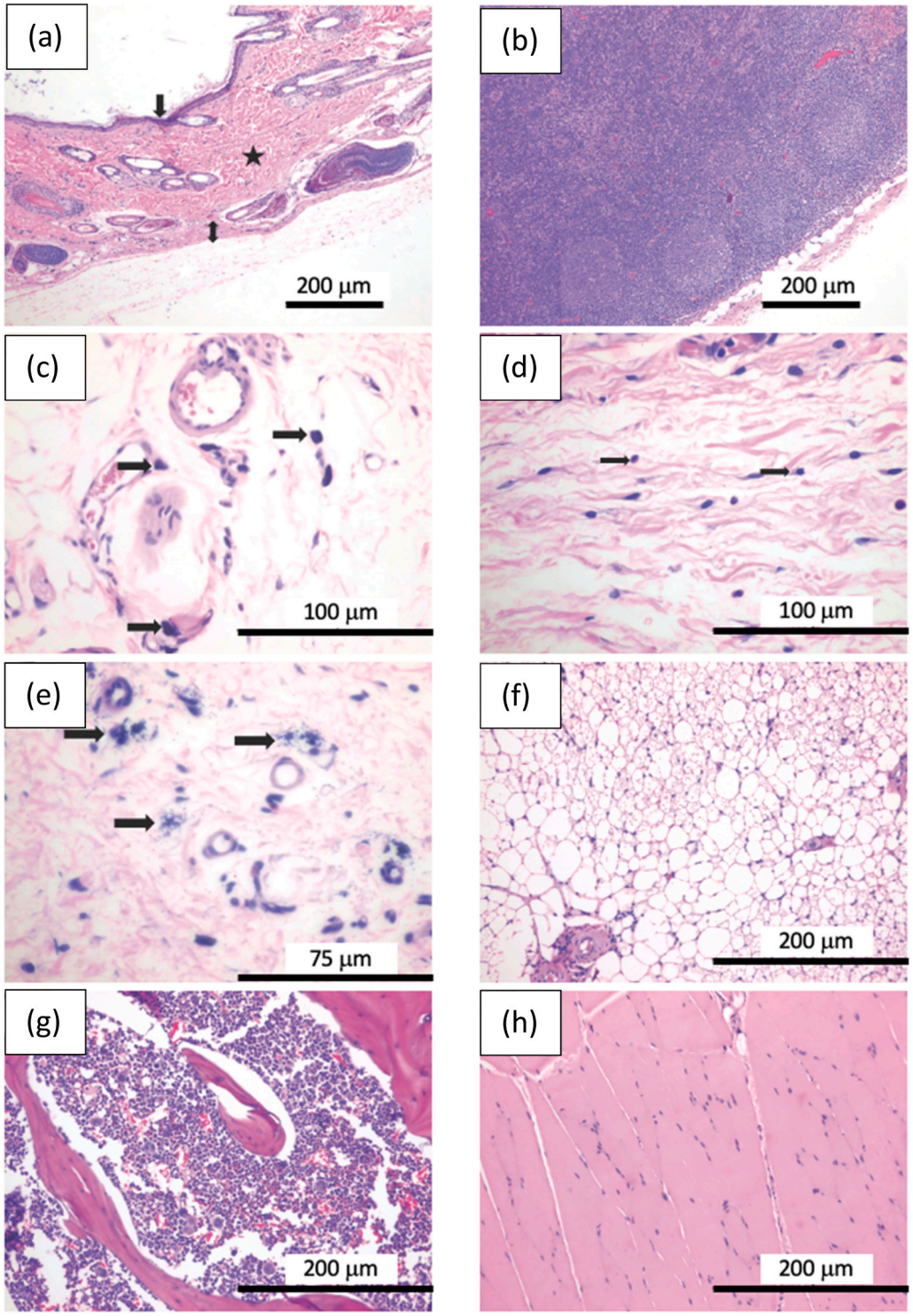

Fig. 9. (a) Section from rat A1 control (cp-Ti) at 12 weeks showing skin epidermis (black arrow), dermis (black star) with underlying capsule (bi-headed arrow), and subcutaneous tissue (white star) (100X, H&E). (b) High power view from rat B1 control (cp-Ti) at 4 weeks, showing a reactive lymph node (100X, H&E). (c) Section from rat C1 control (cp-Ti) at 8 weeks showing multiple mast cells (arrows) (400X, H&E). (d) Section from rat I1 control (cp-Ti) at 12 weeks showing a few neutrophilic bands (arrows) (400X, H&E). (e) Section from rat B2 (the alloy) at 12 weeks showing degranulated mast cells (arrows) (600X, H&E). (f) Section from rat I2 (the alloy) at 8 weeks showing brown fat section (200X, H&E). (g) Section from rat G2 (the alloy) at 12 weeks showing normal bone marrow with normal hematopoiesis (200X, H&E). (h) Section from rat J2 (the alloy) at 8 weeks showing normal skeletal muscles (200X, H&E).

stress shielding and ensuring biocompatibility. Future studies should focus on surface modifications and long-term in vivo assessments to fully validate its clinical potential.

Declaration of competing interest

The authors declare that they have no known competing financial interests or personal relationships that could have appeared to influence the work reported in this paper.

Acknowledgments

This work was partially supported by Japan Society for the Promotion of Science (JSPS) KAKENHI Grant Number 26249104 and 25K01521.

Appendix A. Supplementary data

Supplementary data to this article can be found online at https://doi.org/10.1016/j.jmrt.2025.11.120.

Data availability

The datasets generated and analyzed during the current study are available from the corresponding author upon reasonable request.

References

[1] Zhang LC, Chen LY. A review on biomedical titanium alloys: recent progress and prospect. Adv Eng Mater 2019;21:1801215. https://doi.org/10.1002/adem.201801215.
[2] Geetha M, Singh AK, Asokamani R, Gogia AK. Ti based biomaterials, the ultimate choice for orthopaedic implants – a review. Prog Mater Sci 2009;54(3):397–425. https://doi.org/10.1016/j.pmatsci.2008.06.004.
[3] Niinomi M. Mechanical biocompatibilities of titanium alloys for biomedical applications. J Mech Behav Biomed Mater 2008;1(1):30–42. https://doi.org/10.1016/j.jmbbm.2007.07.001.
[4] Rack HJ, Qazi JI. Titanium alloys for biomedical applications. Mater Sci Eng C 2006;26(8):1269–77. https://doi.org/10.1016/j.msec.2005.08.032.
[5] Chmielewska A, Dean D. The role of stiffness-matching in avoiding stress shielding-induced bone loss and stress concentration-induced skeletal reconstruction device failure. Acta Biomater 2024;173:51–65. https://doi.org/10.1016/j.actbio.2023.11.011.
[6] Brumbauer F, Okamoto NL, Ichitsubo T, Sprengel W, Luckabauer M. Minor additions of Sn suppress the omega phase formation in beta titanium alloys. Acta Mater 2024;262:119466. https://doi.org/10.1016/j.actamat.2023.119466.
[7] Shitara K, Yokota K, Yoshiya M, Umeda J, Kondoh K. First-principles design and experimental validation of β-Ti alloys with high solid-solution strengthening and low elasticities. Mater Sci Eng, A 2022;843:143053. https://doi.org/10.1016/j.msea.2022.143053.
[8] Nocivin A, Raducanu D, Vasile B, Trisca-Rusu C, Cojocaru EM, Dan A, Irimescu R, Cojocaru VD. Tailoring a low young modulus for a beta titanium alloy by combining severe plastic deformation with solution treatment. Materials 2021;14(13):3467. https://doi.org/10.3390/ma14133467.
[9] Tane M, Akita S, Nakano T, Hagihara K, Umakoshi Y, Niinomi M, Mori H, Nakajima H. Low Young's modulus of Ti–Nb–Ta–Zr alloys caused by softening in shear moduli c′ and c44 near lower limit of body-centered cubic phase stability. Acta Mater 2010;58(20):6790–8. https://doi.org/10.1016/j.actamat.2010.09.007.
[10] Lee SH, Todai M, Tane M, Hagihara K, Nakajima H, Nakano T. Biocompatible low Young's modulus achieved by strong crystallographic elastic anisotropy in Ti–15Mo–5Zr–3Al alloy single crystal. J Mech Behav Biomed Mater 2012;14:48–54. https://doi.org/10.1016/j.jmbbm.2012.06.008.
[11] Kim KM, Kim HY, Miyazaki S. Effect of Zr content on phase stability, deformation behavior, and Young's modulus in Ti-Nb-Zr alloys. Materials 2020;13:476. https://doi.org/10.3390/ma13020476.
[12] Zhang J, Fan S, Hao Y, Gozdecki N, Lebrun E, Vermaut P, Portier R, Gloriant T, Laheurte P, Prima F. Influence of equiatomic Zr/Nb substitution on superelastic behavior of Ti-Nb-Zr alloy. Mater Sci Eng, A 2013;563:78–85. https://doi.org/10.1016/j.msea.2012.11.045.
[13] Ozan S, Lin J, Li Y, Ipek R, Wen C. Development of Ti-Nb-Zr alloys with high elastic admissible strain, for temporary orthopedic devices. Acta Biomater 2015;20:176–87. https://doi.org/10.1016/j.actbio.2015.03.023.
[14] Liang SX, Feng XJ, Yin LX, Liu XY, Ma MZ, Liu RP. Development of a new β Ti alloy with low modulus and favorable plasticity for implant material. Mater Sci Eng C 2016;61:338–43. https://doi.org/10.1016/j.msec.2015.12.076.
[15] Hanada S, Masahashi N, Semboshi S, Jung TK. Low Young's modulus of cold groove-rolled β Ti-Nb-Sn alloys for orthopedic applications. Mater Sci Eng, A 2021;802:140645. https://doi.org/10.1016/j.msea.2020.140645.
[16] Li S, Lee W-T, Yeom J-T, Kim JG, Oh JS, Lee T, Liu Y, Nam T-H. Towards bone-like elastic modulus in Ti-Nb-Sn alloys with large recovery strain for biomedical applications. J Alloy Compd 2022;925:166724. https://doi.org/10.1016/j.jallcom.2022.166724.
[17] Hao YL, Li SJ, Sun SY, Zheng CY, Yang R. Elastic deformation behaviour of Ti-24Nb-4Zr-7.9Sn for biomedical applications. Acta Biomater 2007;3:277–86. https://doi.org/10.1016/j.actbio.2006.11.002.
[18] Li S, Kim JH, Kang SW, Kim JH, Nam TH, Yeom JT. Superelastic metastable Ti-Mo-Sn alloys with high elastic admissible strain for potential bio-implant applications. J Mater Sci Technol 2023;163:45–58. https://doi.org/10.1016/j.jmst.2023.01.061.
[19] Kim KM, Al-Zain Y, Yamamoto A, Daher AH, Mansour AT, AlAjlouni JM, Aloweidi AS, Al-Abbadi MA, Kim HY, Miyazaki S. Synthesis and characterization of a Ti–Zr-based alloy with ultralow Young's modulus and excellent biocompatibility. Adv Eng Mater 2022;24(2):2100776. https://doi.org/10.1002/adem.202100776.
[20] Tasaki W, Makioka Y, Miyazaki S, Kim HY. Enhancement of {110}<001> texture by controlling α-phase and achievement of low Young's modulus and high strength in metastable β-type Ti–Zr-based alloys. Adv Eng Mater 2024;26(24):2401402. https://doi.org/10.1002/adem.202401402.
[21] Vicente FB, Correa DR, Donato TA, Arana-Chavez VE, Buzalaf MA, Grandini CR. The influence of small quantities of oxygen in the structure, microstructure, hardness, elasticity modulus and cytocompatibility of Ti–Zr alloys for dental applications. Materials 2014;7(1):542–53. https://doi.org/10.3390/ma7010542.
[22] Martins Jr JR, Araújo RO, Donato TA, Arana-Chavez VE, Buzalaf MA, Grandini CR. Influence of oxygen content and microstructure on the mechanical properties and biocompatibility of Ti–15Mo alloy used for biomedical applications. Materials 2014;7(1):232–43. https://doi.org/10.3390/ma7010232.
[23] Ramarolahy A, Castany P, Prima F, Laheurte P, P′eron I, Gloriant T. Microstructure and mechanical behavior of superelastic Ti-24Nb-0.5O and Ti-24Nb-0.5N biomedical alloys. J Mech Behav Biomed Mater 2012;9:83–90. https://doi.org/10.1016/j.jmbbm.2012.01.017.
[24] Besse M, Castany P, Gloriant T. Mechanisms of deformation in gum metal TNTZ-O and TNTZ titanium alloys: a comparative study on the oxygen influence. Acta Mater 2011;59:5982–8. https://doi.org/10.1016/j.actamat.2011.06.006.
[25] Bartakova S, Malek J, Prachar P. The effect of oxygen addition on microstructure and mechanical properties of various beta-titanium alloys. J Occup Med 2020;72:1656–63. https://doi.org/10.1007/s11837-019-03879-w.
[26] Okamoto NL, Brumbauer F, Luckabauer M, Sprengel W, Abe R, Ichitsubo T. Why is neutral tin addition necessary for biocompatible β-titanium alloys? – synergistic effects of suppressing ω transformations. Acta Mater 2024;273:119968. https://doi.org/10.1016/j.actamat.2024.119968.
[27] Zhao GH, Liang XZ, Kim B, Rivera-Díaz-del-Castillo PE. Modelling strengthening mechanisms in beta-type Ti alloys. Mater Sci Eng, A 2019;756:156–60. https://doi.org/10.1016/j.msea.2019.04.027.
[28] Xie F, Yang H, Huang J, Yu J, He X. Sn content effects on microstructure, mechanical properties and tribological behavior of biomedical Ti–Nb–Sn alloys fabricated by powder metallurgy. Metals 2022;12(2):255. https://doi.org/10.3390/met12020255.
[29] Sarraf M, Rezvani Ghomi E, Alipour S, Ramakrishna S, Sukiman NL. A state-of-the-art review of the fabrication and characteristics of titanium and its alloys for biomedical applications. Bio-Des Manuf 2022;5(2):371–95. https://doi.org/10.1007/s42242-021-00170-3.
[30] Sidhu SS, Singh H, Gepreel MA. A review on alloy design, biological response, and strengthening of β-titanium alloys as biomaterials. Mater Sci Eng C 2021;121:111661. https://doi.org/10.1016/j.msec.2020.111661.
[31] Xiao W, Li Y, Tang H, Zhang X, Wang Y, Zhang X. A β-type titanium alloy with high strength and low elastic modulus achieved by spinodal decomposition. J Alloys Compd 2023;963:171270. https://doi.org/10.1016/j.jallcom.2023.171270.
[32] Zhang X, Xu J, Guo H, Liu Z, Chen Y. Phase field simulation of martensitic transformation in Ti–24Nb–4Zr–8Sn alloy. Smart Mater Manuf 2023;1:100017. https://doi.org/10.1016/j.smmf.2023.100017.
[33] Al-Zain Y, Yamamoto A, AlAjlouni JM, Al-Abbadi MA, Al-Sayyed MR, Aloweidi AS, Kim HY, Miyazaki S. Corrosion behavior, in vitro and in vivo biocompatibility of a newly developed Ti–16Nb–3Mo–1Sn superelastic alloy. Mater Sci Eng C 2019;104:109906. https://doi.org/10.1016/j.msec.2019.109906.
[34] Fu J, Yamamoto A, Kim HY, Hosoda H, Miyazaki S. Novel Ti-base superelastic alloys with large recovery strain and excellent biocompatibility. Acta Biomater 2015;17:56–67. https://doi.org/10.1016/j.actbio.2015.02.001.
[35] Xue P, Li Y, Li K, Zhang D, Zhou C. Superelasticity, corrosion resistance and biocompatibility of the Ti–19Zr–10Nb–1Fe alloy. Mater Sci Eng C 2015;50:179–86. https://doi.org/10.1016/j.msec.2015.02.004.
[36] Nakada H, Numata Y, Sakae T, Okazaki Y, Tanimoto Y, Tamaki H, Katou T, Ookubo A, Kobayashi K, LeGeros RZ. Comparison of bone mineral density and area of newly formed bone around Ti-15%Zr-4%Nb-4%Ta alloy and Ti-6%Al-4%V alloy implants. J Hard Tissue Biol 2008;17:99–108. https://doi.org/10.2485/jhtb.17.99.
[37] Bandyopadhyay A, Mitra I, Goodman SB, Kumar M, Bose S. Improving biocompatibility for next generation of metallic implants. Prog Mater Sci 2023;133:101053. https://doi.org/10.1016/j.pmatsci.2022.101053.
[38] Chen LY, Cui YW, Zhang LC. Recent development in beta titanium alloys for biomedical applications. Met 2020;10(9):1139. https://doi.org/10.3390/met10091139.
[39] Karakurt EM, Cetin Y, Incesu A, Demirtas H, Kaya M, Yildizhan Y, Tosun M, Huang Y. Microstructural, biomechanical, and in vitro studies of Ti–Nb–Zr alloys fabricated by powder metallurgy. Materials 2023;16(12):4240. https://doi.org/10.3390/ma16124240.
[40] ISO 10993-5. Biological evaluation of medical devices — part 5: tests for in vitro cytotoxicity. Geneva: International Organization for Standardization; 2009. 2009.
[41] ISO 10993-2. Biological evaluation of medical devices — part 2: animal welfare requirements. Geneva: International Organization for Standardization; 2022. 2022.
[42] Shi L, Wang L, Duan Y, Lei W, Wang Z, Li J, Fan X, Li X, Li S, Guo Z. The improved biological performance of a novel low elastic modulus implant. PLoS One 2013;8(2):e55015. https://doi.org/10.1371/journal.pone.0055015.
[43] Menzies KL, Jones L. The impact of contact angle on the biocompatibility of biomaterials. Optom Vis Sci 2010;87:387–99. https://doi.org/10.1097/OPX.0b013e3181da863e.
[44] ISO 10993-2. (E) biological evaluation of medical devices—Part 2: animal welfare requirements. 2006.

[45] Boennelycke M, Christensen L, Nielsen LF, Everland H, Lose G. Tissue response to a new type of biomaterial implanted subcutaneously in rats. Int Urogynecol J 2011; 22:191–6. https://doi.org/10.1007/s00192-010-1257-3.
[46] Miura K, Yamada N, Hanada S, Jung TK, Itoi E. The bone tissue compatibility of a new Ti–Nb–Sn alloy with a low Young's modulus. Acta Biomater 2011;7:2320–6. https://doi.org/10.1016/j.actbio.2011.02.008.
[47] Ying DY, Luo LX, Young B, Julian AF. In vivo biocompatibility of a novel ceramic–metal biocomposite. Key Eng Mater 2005;284:807–10. https://dx.doi.org/10.4028/www.scientific.net/KEM.284-286.807.
[48] Morita M, Hashimoto T, Yamauchi K, Suto Y, Homma T, Kimura Y. Evaluation of biocompatibility for titanium–nickel shape memory alloy in vivo and in vitro environments. Mater Trans 2007;48:352–60. https://doi.org/10.2320/matertrans.48.352.
[49] Wenzel RN. Resistance of solid surfaces to wetting by water. Ind Eng Chem 1936; 28(8):988–94. https://doi.org/10.1021/ie50320a024.
[50] Majhy B, Priyadarshini P, Sen AK. Effect of surface energy and roughness on cell adhesion and growth – facile surface modification for enhanced cell culture. RSC Adv 2021;11(25):15467–76. https://doi.org/10.1039/D1RA02402G.
[51] Akimoto T, Ueno T, Tsutsumi Y, Doi H, Hanawa T. Evaluation of corrosion resistance of implant-use Ti-Zr binary alloys with a range of compositions. J Biomed Mater Res, Part B 2018;106B:73–9. https://doi.org/10.1002/jbm.b.33811.
[52] Cordeiro JM, Beline T, Ribeiro ALR, Rangel EC, da Cruz NC, Landers R, Faverani LP, Vaz LG, Fais LMG, Vicente FB, Grandini CR, Mathew MT, Sukotjo C, Barão VAR. Development of binary and ternary titanium alloys for dental implants. Dent Mater 2017;33:1244–57. https://doi.org/10.1016/j.dental.2017.07.013.
[53] Tan T, Zhao Q, Kuwae H, Ueno T, Chen P, Tsutsumi Y, Mizuno J, Hanawa T, Wakabayasi N. Surface properties and biocompatibility of sandblasted and acid-etched titanium–zirconium binary alloys with various compositions. Dental Mater J 2022;41(2):266–72. https://doi.org/10.4012/dmj.2021-210.
[54] Xie F, Lu D, Cao S, Mu Y, Sun Q. Electrochemical corrosion behavior and in vitro biocompatibility of Ti-Nb-Sn alloy for dental applications. Corros Sci 2023;224: 111531. https://doi.org/10.1016/j.corsci.2023.111531.
[55] Torres-Sanchez C, Norrito M, Wang J, Bell H, Zani L, Conway PP. Physico-chemical characterisation of Ti-Nb-Sn alloys surfaces and their osteogenic properties. Surf Coating Technol 2020;43:126439. https://doi.org/10.1016/j.surfcoat.2020.126439.
[56] Tamada Y, Ikada Y. Cell adhesion to plasma-treated polymer surfaces. Polymer 1993;34(10):2208–12.
[57] Park YJ, Song YH, Ana JH, Song HJ, Anusavice KJ. Cytocompatibility of pure metals and experimental binary titanium alloys for implant materials. J Dent 2013; 41:1251–8. https://doi.org/10.1016/j.jdent.2013.09.003.